Article

Diurnal Variations of Surface and Air Temperatures on the Urban Streets in Seoul, Korea: An Observational Analysis during BBMEX Campaign

Yoo-Jun Kim [1,*], Joon-Bum Jee [2], Geon-Tae Kim [1], Hyoung-Gu Nam [1], Jeong-Sun Lee [1] and Baek-Jo Kim [1]

[1]   High Impact Weather Research Center, National Institute of Meteorological Sciences, Gangneung 25457, Korea; gtkim@korea.kr (G.-T.K.); hyounggu@korea.kr (H.-G.N.); jsunee@korea.kr (J.-S.L.); bjkim@kma.go.kr (B.-J.K.)

[2]   Research Center for Atmospheric Environment, Hankuk University of Foreign Studies, Yongin 17035, Korea; rokmcjjb717@gmail.com

*   Correspondence: yoojun@korea.kr; Tel.: +82-33-913-1052

check for updates

Abstract: In this study, we used an intensive observation dataset of a mobile observation vehicle (MOVE) to investigate the characteristics of thermal environments and diurnal variations of road surface temperature (RST) and air temperature, particularly at the urban street level, during the 2019 Building Block 3-dimensional urban Meteorological Experiment (BBMEX) campaign in Seoul. For the purpose of comparing characteristics of RST and air temperature with different surrounding thermal environments, we divided the road into four sections (S1: Open Section, S2: High-Rise Buildings, S3: Low-Rise Buildings, S4: Street Trees). This study demonstrates that the greater sky view factors (SVFs) are generally coincident with the greater RSTs, with a significance at the 5% level. The diurnal variations indicated that the time lag between observed maximum air temperature and RST has about one hour, which is attributable to an increase air temperatures above artificial pavement through heat convection with some latency. The diurnal temperature ranges (DTRs) of RST in S2 and S4 were relatively smaller than those of S1 and S3, with differences ranging from 2.9 °C to 4.5 °C. The current results will assist planners and decision makers in determining policy priorities with regard to urban street design and planning.

Keywords: mobile observation vehicle; road surface temperature; sky view factor; diurnal temperature range

1. Introduction

Heat waves are one of the major meteorological disasters, because they can affect many aspects of human society, including through their impacts on socio-economics, health, and drought [1–3]. Urban areas, particularly dense cities, are more susceptible to the impacts of heat waves [4,5], and thus the increase in air temperatures can be accelerated compared to suburban or rural areas by adding urban heat island (UHI) effects and the tropical night phenomenon [6]. In addition, the increase in temperature also affects road-surface temperature (RST), which is an important research topic in terms of extreme road weather [7–9]. In the summertime, high surface temperatures can cause asphalt melting, tire blowouts, and deformation induced by thermal stress on the roads [7].

There have been lots of studies on UHI effects in densely built-up areas from street thermal environment investigation include numerical simulation, Landsat, thermal imaging camera, car-traverse mobile measurement. Bae et al. (2012) [10] proposed planning schemes, such as type and organization of building and location of green space and circulation, to alleviate the UHI effect through learning

from simulations. Chung and Park (2016) [11] showed that the phase change materials doped tiles effect a temperature decrease in surface temperature while keeping the chamber temperature low in summer weather condition. Jeong and Chung (2017) [12] suggested that the effect of temperature reduction on the roof layer of buildings is more effective than adjusting the reflectivity of building, through simulating the UHI reduction factor by types of complex.

However, most previous studies have been conducted based on numerical modeling of urban morphologies such as buildings, roofs, and other materials, while few observational studies have considered the impact of the thermal environmental characteristics of urban street elements on surface temperatures using a thermal imaging camera. Yamazaki et al. (2009) [13] found that areas with roadside trees and road-center plants were cooler than areas of pavement or building walls. Yoon (2009) [14] showed that the surface temperatures of asphalt pavement were higher than those of vegetated areas or sidewalk blocks around an artificial fountain. Lee et al. (2018) [15] suggested that street trees were the most effective mitigation element for reducing surface temperatures, and the temperatures of artificial turf or wooden decks on urban streets are also significantly high during the daytime. Even though these studies analyzed urban surface temperatures using a thermal imaging camera, they are limited insofar as they focused specifically at the pedestrian level, which is a relatively micro-scale analysis.

In addition, numerous studies on UHI effects have examined relationships between land use/land cover (LULC) and land surface temperature (LST) [16–20]. Zhao et al. (2017) [18] examined the typical characteristics of LST in summertime and temperature variations over all LULC types using Landsat 8 imagery. He et al. (2019) [20] investigated how background temperature affects performances of cool/hot sources in either enhancing or mitigating LST in Shenyang, China based on Landsat 8 imagery. However, Landsat 8 thermal images often do not provide sufficient accuracy and temporal resolution because the satellite passes through a specific area only twice in each month (fortnightly). From the ground observation point of view, data from the road weather information system (RWIS) provides continuous information about the RST together with information about atmospheric conditions, such as air temperature and humidity, at different sensor locations. Despite progress in many investigations using RWIS data worldwide [21–23], the performance of the RST prediction model is still limited in areas with sparse observations [24]. Therefore, a well-designed observation framework based on mobile platforms equipped with both road-surface and meteorological sensors is required to capture accurate road-weather information with high spatial and temporal resolutions in vulnerable regions [9].

Kim et al. (2019) [9] recently investigated the characteristics of road-surface and air temperatures using a Mobile Observation Vehicle (MOVE) dataset for the heat wave episode that occurred on 16–17 August 2018 in Seoul. However, the study addressed thermal behavior in only a specific (the warmest) time on different urban streets, and diurnal variations of urban RST and air temperature still remain poorly resolved [25–27]. Furthermore, a greater variety of factors and different environmental indices such as sky view factor (SVF) should be considered using a quantitative method in further research [28–30]. In 2018, the highest air temperature recorded in Seoul, the capital city of Korea, since the government started compiling the data in 1907, was 39.6 °C (Korea Meteorological Administration), and at the time of writing 48 people had died of heat stroke in Korea (Korea Centres for Disease Control and Prevention). Although heat waves (and/or UHI effects) and road weather are inextricably linked, and have socioeconomic impacts, there have been very few studies that have combined these topics. Therefore, the purpose of this study is to investigate the characteristics of thermal environments and diurnal variations of RST and air temperature, particularly at the urban street level, during the 2019 Building Block 3-dimensional urban Meteorological Experiment (BBMEX) campaign in Seoul. A MOVE dataset, with the high spatial and temporal resolutions for the heat wave episode that occurred on 5–6 August 2019, was used to analyze the relationship between RST and SVF, and other relevant factors in terms of field observational analysis.

2. Data and Methods

2.1. Study Area

Seoul is not only the provincial capital city, but also the largest metropolis of South Korea (Figure 1). It is in the northwest of South Korea, and its area comprises 605.25 km^2, with a radius of approximately 15 km, roughly bisected into northern and southern halves by the Han River. The suburbs of Seoul are generally cooler than the center of Seoul because of the urban heat island (UHI) effect. Summers are generally hot and humid, with the East Asian monsoon taking place from June until September. August, the hottest month, has average high and low temperatures of 32.6 °C and 23.4 °C, with higher temperatures possible.

A mobile observation vehicle (MOVE) was driven on major roads (from point A to point J) around Gwanghwamun of Seoul city during the Building Block 3-dimensional urban Meteorological Experiment (BBMEX) campaign, as shown in Figure 1 and Table 1. To compare characteristics of RST and air temperature with different surrounding thermal environments, we divided it into four road sections (S1: Open Section, S2: High-Rise Buildings, S3: Low-Rise Buildings, S4: Street Trees). Representative road spots are shown in Figures 1 and 2, and the sections for analysis were divided as follows: S1 (point C to F or point I to J, alphabet 'T' shape), S2 (point A to C), S3 (point G to H or point J to A), and S4 (point H to I) in Figure 1. These roads are adjacent, so they are considered to experience the same climate conditions [15]. Various environmental characteristics are found on each road, even though they are all core urban streets of Seoul. Building heights, density of street trees, road width, and degree of sky openness are the representative characteristics of each road (Figure 2). Sejong-daero has the largest road width in South Korea, and it is also high in sky openness compared to the other roads in our area of study. Jong-ro 5-gil has a high concentration of high-rise buildings, such as the Grand Seoul and Samgong building, which are over 20 m (Figure 1), whereas relatively low-rise buildings (small clothing stores and restaurants) are mainly located in Saemunan-ro 5-gil A. Finally, on the Saemunan-ro 5-gil B, even though there are a few high-rise buildings, a greater amount of street trees can be seen along the road compared to the other urban streets.
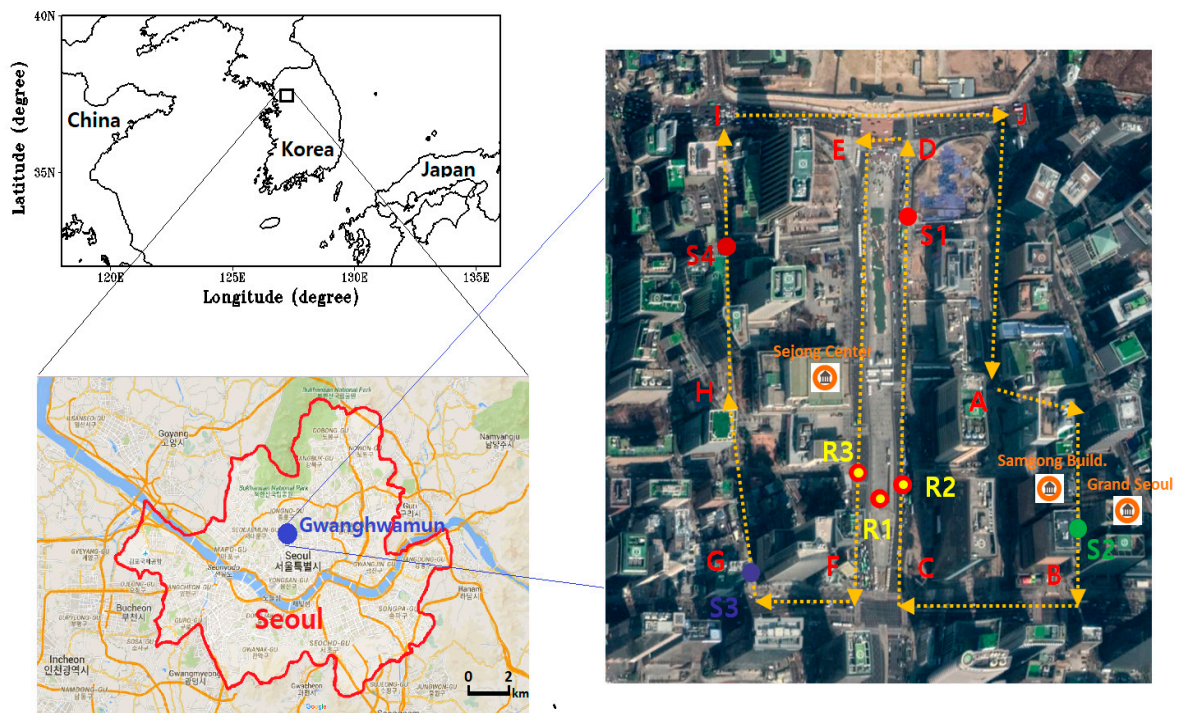

Figure 1. Map of the study area—Gwanghwamun, Seoul.

Table 1. Summary of observation roads during the BBMEX campaign.

Road Sections	Road Names	Remarks
A→B	Jong-ro 5-gil	-
B→C	Jong-ro	-
C→D	Sejong-daero	-
D→E	Sajik-ro	Traffic light (U-turn)
E→F	Sejong-daero	-
F→G	Saemunan-ro	-
G→H	Saemunan-ro 5-gil	-
H→I	Saemunan-ro 5-gil	One way, Traffic light
I→J	Sajik-ro	Traffic light
J→A	Jong-ro 1-gil	-

Figure 2. Four urban streets around Gwanghwamun, Seoul. Each road corresponds to the closed circle with separated color marked in Figure 1.

2.2. MOVE Dataset

Seoul has the highest traffic volume in Korea, but only a small number of road weather information system (RWIS) sites. Meteorological factors such as air temperature, wind, solar radiation and humidity are also important for predicting road-surface temperature [31,32]. Therefore, road weather observations by using MOVE could be useful for urban meteorology studies. The MOVE datasets used in this study were generated by equipment including road weather sensors and a temperature/humidity probe and radiation sensors. A detailed schematic diagram of MOVE and information on the instruments are presented in Figure 3 and Table 2, respectively [9]. All data were collected at a 1-s rate, were displayed in real time, and transmitted to a server within 5 min using machine-to-machine technology. Quality-checked algorithms were used for data-processing based on the MOVE platform [33]. The data were interpolated at about 40 m (5-s) intervals to smooth the spatial distribution of each variable. The detailed descriptions of MOVE dataset are presented in Table 2 and are also explained in Kim et al. (2019) [9,34,35].

Table 2. Overview of observational instruments from MOVE platform.

Instruments *	Variables	Precisions	Manufacture (Model)
Sport Utility Vehicle	Vehicle Speed	-	Hyundai (Maxcruz)
Ultrasonic Wind Sensor	Wind Speed/Wind Direction	± 0.2 m s^{-1}	Vaisala (WMT703)
GNSS Antenna	Latitude/Longitude, Altitude	>3 m	Trimble (NetR9)
Rain Detector	Rain Signal	± 1 min	Vaisala (DRD11A)
Barometer	Pressure	± 0.1 hPa	Vaisala (PTB330)
Temp./Humidity Probe	Air temperature/Humidity	± 0.22 °C/± 3%	Vaisala (HMP155)
Rain Gauge	Precipitation	± 3%	Vaisala (RG13H)
Road Weather Sensors	Surface Temperature	± 0.28 °C	Vaisala (DSP101, DSC111)
Net Radiometer	SW/LW Radiation	<1%	Kipp&Zonen (CNR4)
Pyranometer	Solar Radiation (Insolation)	<3%	Kipp&Zonen (CMP11)

* Each number corresponds to the equipment number shown in Figure 3.
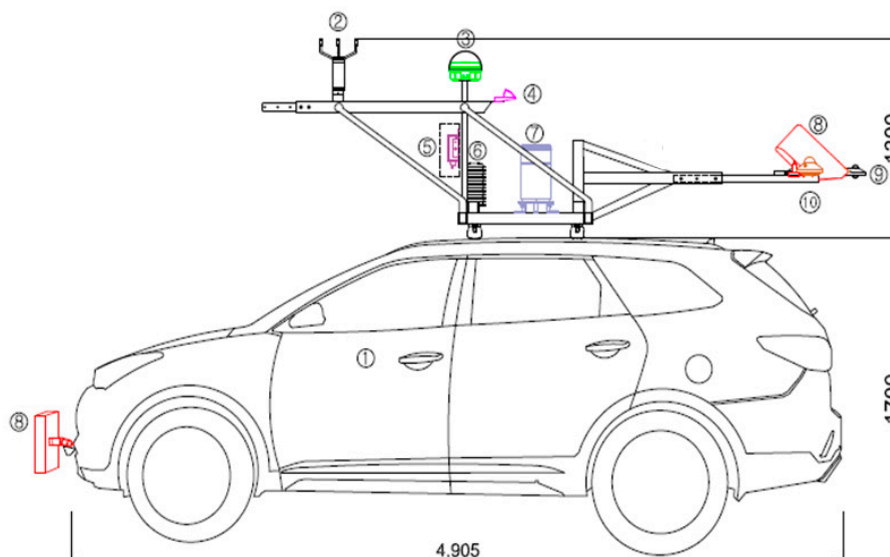
Figure 3. Detailed schematic diagram of the Mobile Observation Vehicle (MOVE) equipped with road weather and meteorological sensors (obtained from Kim et al., 2019 [9]).

2.3. BBMEX and Environmental Parameters

The BBMEX campaign was carried out starting from 2019 to understand the correct distribution of weather fields around urban building blocks. Here, we discuss the heat-wave episode that occurred on 5–6 August 2019 (BBMEX campaign) above four road sections. To minimize the impact of additional heat from the internal combustion engine of nearby vehicles, we kept enough distance, and the cruise control was set at about 30 km h^{-1}, except in traffic light segments (Table 1). In addition, to avoid the impacts of shade or sunlight due to lane direction, we drove as close to the center line as possible. During the BBMEX campaign, traffic flow was generally good, without traffic congestion except for short stops (below 2 min) due to red lights. The total distance of the observation route per cycle was 3.2 km (about 12 min). To ascertain the accuracy of the MOVE datasets during the observation times, we compared 1-s air temperature values from MOVE with those of 1 min obtained with 2 fixed complex weather sensors (Hankook University of Foreign Studies, HUFS) installed at points R2 and R3 in Figure 1.

We propose sky view factor (SVF) and specific humidity as environmental parameters. Three-dimensional urban factors that reflect the urban geometry could be important in analyzing the UHI phenomenon in metropolitan areas [36]. In particular, the SVF has an important role in the analysis of the urban micro-climate [37]. Therefore, in this study, SVF was used to explain the differences in RST and air temperature with different four sections. First, the digital surface model

(DSM) data with 10-m spatial resolution used in this study provides gridded altitude (m), slope and aspect information, and reflects the height of artificial structures unlike digital elevation model (DEM), which do not reflect the influence of surrounding trees and buildings. Since SVF computed using 3-dimensional geometry dataset (altitude and sky line) is retrieved as Cartesian coordinates centered on the zenith, Equations (1) and (2) are converted into a spherical coordinate system:

$$x = r \, \sin \alpha \, \cos \varnothing, \tag{1}$$

$$y = r \, \sin \alpha \, \sin \varnothing, \tag{2}$$

where x and y represent grid points (latitude and longitude) of DSM data, respectively, r is the distance between grids of the DSM data, and α and $\varnothing$ are the elevation and azimuth angles for the sky line, respectively. The SVF can be calculated as shown in Equation (3) by using the altitude angle of the sky line for each azimuth angle [37,38]:

$$SVF = \frac{1}{2\pi} \int_{\varnothing=0}^{2\pi} \sin^2 \theta d\varnothing, \tag{3}$$

where θ ($90° - \alpha$) denotes the zenith angle. One of the geometric properties, called SVF, defines the ratio of sky hemisphere visible from the ground. If SVF is one, the sky area is not shielded by obstacles such as buildings, terrain or trees, and the closer to zero, the more the sky area is blocked by the obstacles.

On the other hand, humidity can also act as local forcing on RST and air temperature through evaporative cooling, which is effective during the day when the planetary boundary is unstable. Therefore, in this study, we analyzed specific humidity to quantify the effects of this hydrological variable on those temperatures. Specific humidity (q) can be calculated as shown in Equations (4) and (5) [39]:

$$q = 0.622 \left(\frac{e}{p - (1 - 0.622) \, e} \right), \tag{4}$$

$$e_s = 6.112 \cdot \exp \left(\frac{(17.67 \cdot T_a)}{(T_a + 243.5)} \right), \tag{5}$$

where atmospheric pressure (p) and air temperature (T_a) were obtained with PTB330 and HMP155 sensors (Vaisala, Finland) of MOVE at 2.2 m altitude (Table 2 and Figure 3), and vapor pressure (e) can be retrieved using the relative humidity data of MOVE and the relationship in Equation (5). Specific humidity, the mass of water vapor in a unit mass of moist air (g kg^{-1}), is a useful quantity in meteorology and does not vary as the temperature or pressure of a body of air changes, as long as moisture is not added to or taken away from it.

3. Data Validation

To confirm the quality of the MOVE data and to ascertain the data accuracy of the fixed sites, we used air temperature data from 2 fixed complex weather sensors (Hankook University of Foreign Studies, HUFS) installed at points R2 and R3 (Figure 1) during the observation period of the MOVE. MOVE data were collected for 17 (32 cycles) repetitive observations from 1451 local standard time (LST), 5 August to 2059 LST, 6 August (Table 3). Considering that validation time does not always coincide with the temporal resolution (1 min) of 2 fixed weather sensors, we retrieved a 1-min interval for MOVE data, and air temperature values from MOVE within a radius of 20 m of fixed sites were extracted. We compared air temperature values from MOVE with those of 2 fixed weather sensors. A scatter plot for the 32 cycles is shown in Figure 4a. As a result, the linear relationship (slope = 0.98) and coefficient of determination ($R^2 = 0.94$) show good agreement, although the mean bias (-0.36 °C) tended to be slightly negative. These results demonstrated that the accuracy of air temperature data from MOVE is quite reliable under moving conditions on urban streets. However, validation of road

surface temperature (RST) on a MOVE platform was difficult, because there were no road weather information system (RWIS) sites in the study area.

Table 3. Summary of observation times during the BBMEX campaign.

Date	Start Time (LST *)	End Time (LST)	Return Time ** (LST)
5 August 2019	14:51:00	15:15:45	15:05:39
	15:48:00	16:17:29	16:02:05
	17:48:01	18:17:39	18:01:46
	19:48:01	20:16:50	20:01:49
	20:48:01	21:14:09	20:59:55
6 August 2019	06:48:00	07:16:01	07:01:46
	07:54:00	08:06:56	1 cycle
	08:48:00	09:18:20	09:04:40
	09:47:00	10:15:00	10:00:50
	10:48:00	11:15:00	11:01:50
	11:48:00	12:20:01	12:05:30
	14:47:00	15:14:29	15:01:19
	15:47:00	16:21:40	16:02:19
	16:47:00	17:04:49	1 cycle
	17:47:00	18:20:19	18:05:09
	19:47:00	20:16:39	20:02:49
	20:47:01	21:14:02	20:59:01

* Local Standard Time (HH:MM:SS), ** Start time of 2nd cycle except for 1 cycle observation.

Figure 4b shows the time series of air temperature along with wind speed and wind direction at site R1 (Gwanghwamun Square) during the observation period of MOVE. Compared to Seoul AWS about 1 km away, the maximum air temperature (38.5 °C) was about 2 °C higher at 1450 LST, 6 August despite the short distance, whereas the minimum air temperature was 29.3 °C at 0540 LST (6 August), which meets the level (greater than 25 °C in daily minimum air temperature) of tropical night phenomenon (Korea Meteorological Administration). In this study, the R1, the hottest spot in Seoul, was selected as the reference site for the comparison with air temperatures of MOVE at each different section. The focuses of the surrounding wind environment are wind speed and wind direction, forming the nearest boundary conditions of the precinct [40]. In this regard, the local wind at site R1 was chosen as the representative wind, because it is an open space that is less influenced by the urban morphological characteristics. During the Building Block 3-dimensional urban Meteorological Experiment (BBMEX) campaign, the average wind speed was weak at 1.1 m s^{-1}, and there was predominant northerly or easterly wind flow (Figure 4b). Therefore, the ventilation effects on the urban streets due to surrounding wind environments can be minimized.

Sky view factor (SVF) can be calculated from the DSM [41–43], but direct measurement of SVF from three-dimensional (3D) sky image is also necessary [44]. Therefore, SVF values based on DSM data used in this study need to be verified with SVF using 3D cameras. During the BBMEX campaign, a total of 18 3D cameras were installed and photographed near Gwanghwamun Square (in the section of C to F in Figure 1). After setting the horizontal plane based on the center of observation point, the 3D camera images can be calculated using the image processing technique and SVF calculation methods [38]. The SVF values using the DSM data (as presented in Section 2.3) were compared with those values using 3D sky image. Jee et al. (2019) [45] suggested reasonable results of SVF based on DSM data except for the point (Sejong Center for the Performing Arts as shown in Figure 1), in which information regarding surface characteristics was not reflected well. The high-spatial-resolution (10-m) dataset of SVF during the BBMEX campaign is used to characterize the geometry of urban canyons and thermal environments for the four different sections in the study area.
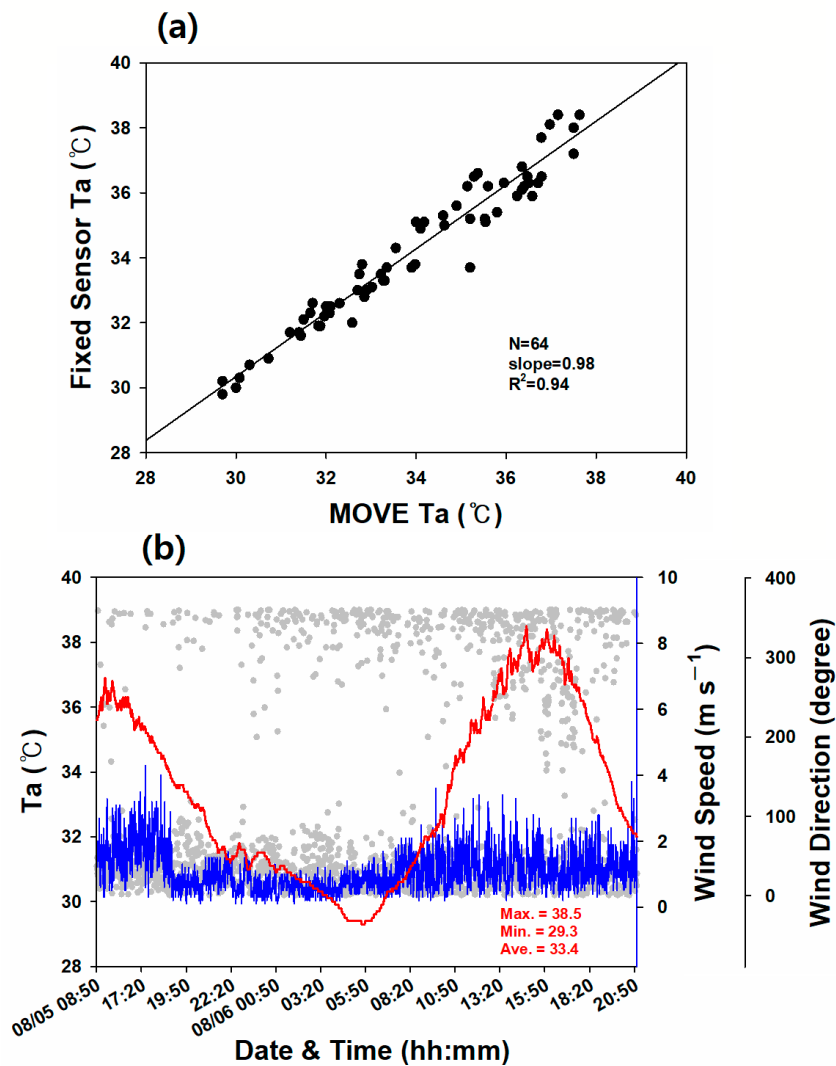
Figure 4. (**a**) Comparison between air temperatures from two fixed sensors (R2 and R3) and MOVE, and (**b**) time series of air temperature (left axis), wind speed and wind direction (right axis) at site R1, as marked in Figure 1 during the observation period of MOVE.

4. Results

4.1. Synoptic Analysis

We analyze the synoptic conditions for the heat wave episode selected in this study. Figure 5a,b show the 200 hPa and surface weather chart at 0000 UTC 5 August 2019. At 200 hPa, the Tibetan High was a strong and steady atmospheric anticyclone in summer (Figure 5a). In particular, it had a great impact on the summer heat waves in East Asia. In the surface weather chart, the North Pacific High stretches westward to the edge of the Korean Peninsula (Figure 5b). It is pointed out that the North Pacific High strengthened and extended westward, when the Tibetan High strengthened and moved eastward. This characteristic of circulation patterns eventually results in the trapping of heat wave with massive layer of high pressure. This implies that the adiabatic heating induced by subsidence makes great contributions to heat waves in Korea.

Additionally, Korea is dominated by warm water vapor associated with the influence of the 8th Typhoon 'Francisco' (Figure 5c). Consequently, Seoul, located on the western side of the Korean Peninsula, was added to the impact of the Typhoon, and synoptic conditions were formed to accelerate the heat wave. Persistent subsidence and adiabatic warming can cause severe heat waves over Korea.

Figure 5d presents spatial distribution of daily maximum air temperatures at 1.5 m from Automatic Weather Stations (AWS) operated by the Korea Meteorological Administration (KMA). The observed air temperature was interpolated using 704 surface AWS in Korea. Horizontal distribution of air temperatures showed a strong difference between inland and coastal areas of the Korean Peninsula. The maximum temperature of Seoul AWS (located in Songwol-dong), which is the closest to the study area, was 35.9 °C (15:30 LST), and on August 6, the next day, the temperature rose to 36.8 °C (14:50 LST). The episode selected for this study is the hottest period in 2019, and exceeded the level of heat wave warning (greater than 35 °C in daily maximum air temperature) in Seoul. In this study, a total of 17 (32 cycles) repetitive observations, including both daytime and nighttime, were performed using the MOVE platform on the main roads around Gwanghwamun, Seoul, in order to investigate the characteristics of diurnal changes in RST and air temperature during the BBMEX campaign (5–6 August 2019). A detailed observational schedule is summarized in Table 3. It was performed in two cycles per observation to increase the number of sampling and representativeness of data except for the two time zones on 6 August.
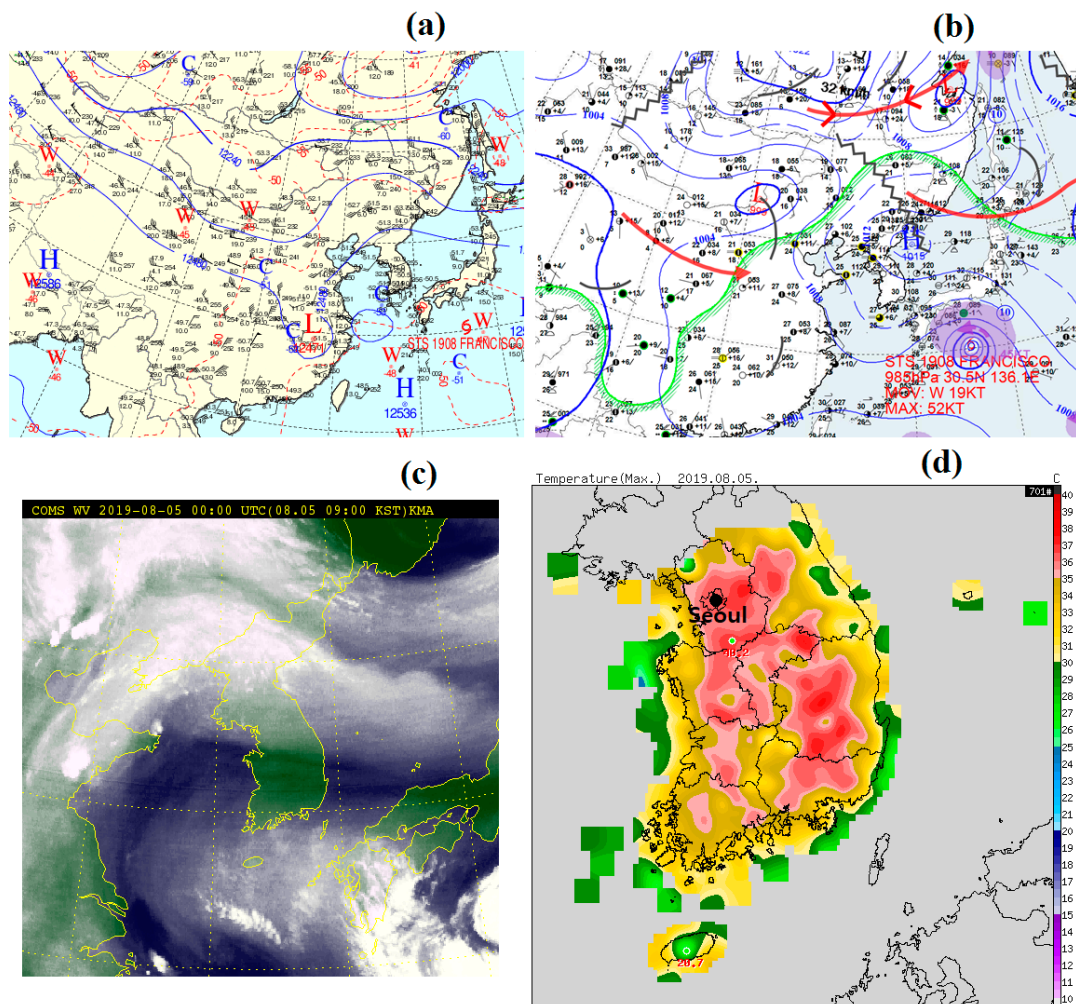

Figure 5. (**a**) 200 hPa and (**b**) surface weather chart, and (**c**) Communication, Oceanic and Meteorological Satellite (COMS) water vapor image at 0000 UTC, and (**d**) spatial distribution of daily maximum air temperatures on 5 August 2019.

4.2. RST Distributions over the Study Area

Figure 6a shows the spatial distribution of road surface temperature (RST) during the hottest time (from 1547 to 1602 LST on 6 August) of the BBMEX period, which was measured using a surface patrol

infrared sensor of MOVE. The highest RST was mainly observed on the road of Section 1 (S1; alphabet 'T' shape), with a maximum RST of 52.8 °C. In contrast, the lowest temperature was measured on the roads of Section 2 (S2) and Section 4 (S4), with a minimum RST of 35.2 °C. The reasons for the higher and lower RSTs on the MOVE platform were due to the different surrounding environments of the urban streets. Open skies are mainly found on the roads with higher RST, and high-rise buildings were easily observed to be on the roads with lower RST, such as Sejong-daero and Jong-ro 5-gil, as shown in Figure 2. In other words, the thermal environment can increase RST, which is determined by the degree of sky openness and building density, etc. The spatial distribution of air temperature is compared with that of RST (Figure 6a,b). It is interesting to note that the distributions of RST and air temperature were consistent. Air temperature showed a maximum (38.7 °C) on the road spot of Gwanghwamun entrance (red triangle marked in Figure 6b), which may be attributable to the additional heat from the internal combustion engine of the vehicles that were waiting at the red light (Figure 1 and Table 1). The minimum air temperature (35.8 °C) was observed on the road spot around KT Gwanghwamun building–East. Despite the similarity of RST and air temperature distributions, the magnitude of RST difference (17.6 °C) was about six times higher than that of air temperature (2.9 °C), which means that the RST distribution was more sensitive and variable according to the different thermal environments around the urban streets.
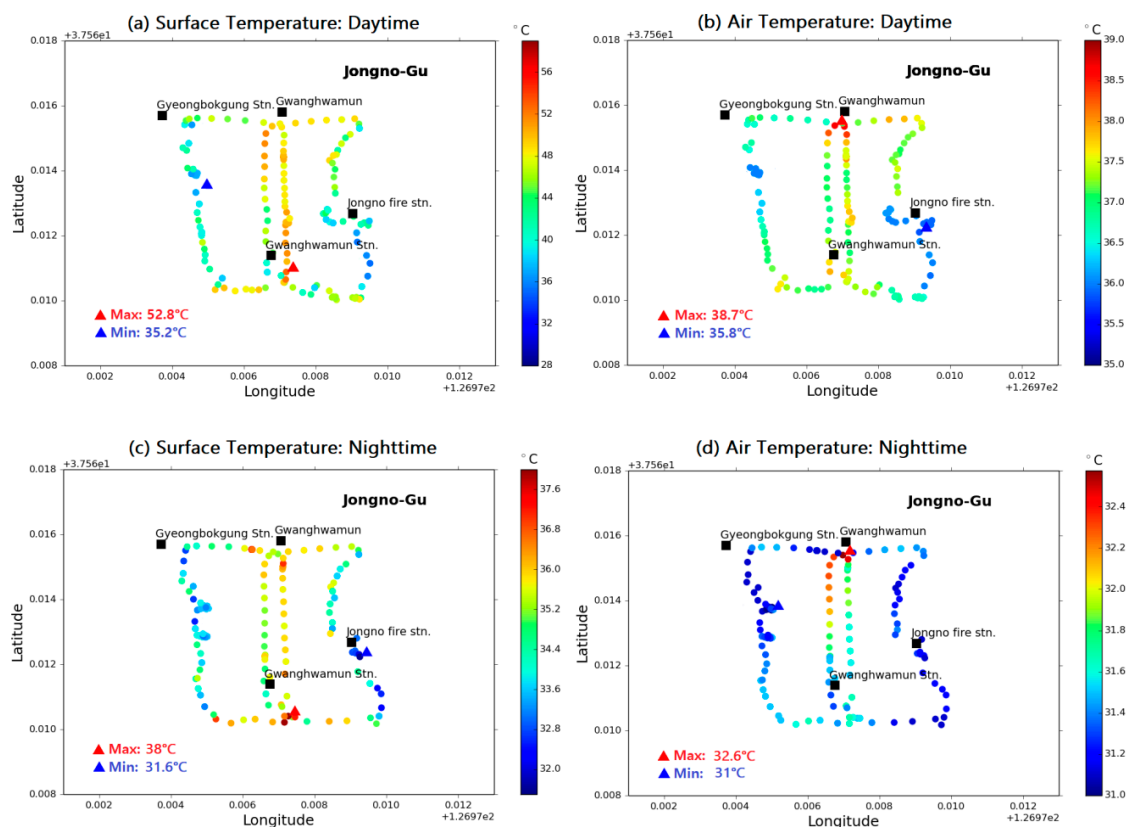
Figure 6. Spatial distributions of road surface temperature (RST) and air temperature from MOVE observations during the (**a**,**b**) daytime (1547–1602 LST) and (**c**,**d**) nighttime (2047–2114 LST) on 6 August, 2019. The color bars represent different temperature ranges.

As indicated, there was a tropical night phenomenon where the air temperature remained above 25 °C even at night during the BBMEX campaign. Therefore, we also examined the distributions of RST and air temperature at nighttime. Figure 6c shows the spatial distribution of RST at nighttime (from 2047 to 2114 LST) on the same day. Here, we detected abrupt change in RST distribution especially in S2 and S4, which is susceptible to signal loss (error in position estimation) due to obstructions around the road such as a high-rise building, a roadside tree, or other features [35]. The signature

of the RST field at nighttime exhibited a result similar to that of the spatial distribution of RST at daytime (Figure 6a,c), which means that the differential heating on the road surface according to the section was maintained continuously until nighttime. However, the temperature range of nighttime RST was reduced by about 11 °C (36%) compared to that of daytime due to the blocking of the surface heating by the sun. In addition, the RST showed a tendency that the east–west section was higher than the south–north section, except for Sejong-daero in S1. On the other hand, we found that the differences between maximum and minimum air temperatures at nighttime were reduced to within 1.6 °C (Figure 6d), which is thought to be associated with lower ambient air temperature than the RST due to nighttime radiative cooling. It is interesting to note that the distribution of air temperature on Sejong-daero was about 1 °C higher at the same observation time. In the end, we suggest that the urban street width and sky openness contributes significantly to the magnitude of RST and air temperature for the whole day.

4.3. Comparison of the Factors Influencing RST

In this section, the screening impact of urban canopy such as buildings and street trees influencing the RST during the heat wave in Jongno-gu, one of the areas with the highest urban canopy layer in Seoul, is examined, and the combined MOVE dataset and digital surface model (DSM) data are used to investigate how solar radiation and SVF are related to RST. Figure 7a shows the spatial distribution of solar radiation at the same time as Figure 6a,b. The result is compared with that of RST during daytime, as shown in Figure 6a. As a result, we found the distribution of solar radiation to have comparatively similar patterns; however, there is disagreement (negative difference) in the section of Saemunan-ro 5-gil located on the western side (north–south direction) road with those of RST (Figures 6a and 7a). To confirm the relationship between solar radiation and spatial structure in the vicinity of Saemunan-ro 5-gil (point A; Government Complex–Seoul, as marked in Figure 7a), we also examined a 3D map from the Vworld web service, as shown in Figure 7b. The open-platform-based Vworld map service is operated under the sponsorship of the Ministry of Land, Transport and Maritime Affairs in Korea. A 3D map view in the section of Saemunan-ro 5-gil shows concentrations of high-rise buildings on the left side of road. In this regard, we considered that the decreases in solar radiation in that section were affected by the shielding due to high-rise buildings on the left side of the driving direction. In addition to that, the solar azimuth and elevation angles mainly describe the lowest solar radiation measured on the road. According to the Korea Astronomy and Space Science Institute, the solar azimuth and elevation angles were 259° and 41° at 1600 LST of point A, respectively, so the exposed solar radiation area was smaller on the Saemunan-ro 5-gil (around 70 W m^{-2}) than on the Sejong-daero with maximum solar radiation up to 549 W m^{-2}. That is, it is suggested that the magnitude of incoming solar radiation is mainly dependent on the arrangement of high-rise buildings associated with diurnal variations in solar azimuth and elevation angles.

SVF is one of major importance for urban meteorology applications since the long-wave radiation term emitted by built surface to the sky is directly impacted by its value [37], thereby influencing the RST. To obtain an accurate SVF value to each section of urban streets, it should be calculated for a high number of points. Herein we retrieved the SVF using the digital surface model (DSM) dataset with 10 m resolution as shown in Section 2.3. Figure 8a shows the SVF distribution based on DSM dataset in the study area. We identified a significant difference in SVF between suburban area located in the northern part above 37.576° N and dense urban area populated by tall buildings except for the Sejong-daero section, and a relatively small SVF in urban canyon among high-rise buildings, which means that the lower SVF is mainly caused by screening impacts according to the urban canopy. For the detailed analysis in different road sections selected in this study, the SVF values were only drawn for MOVE's observation path in the domain (Figure 8b). Interestingly, the results show that the SVF distribution is associated with the features of RST distribution. The highest SVF (0.96) was observed on S1 ('T' shape) including Sejong-daero, where most parts of the road were open sky which is less affected by the surrounding structures, whereas the lowest SVF (0.20) was measured on S2,

due to dense high-rise buildings that could affect the ratio of sky hemisphere visible at road spot. In comparing the RST distributions of the four sections, the SVF values overall succeed in capturing the spatial pattern of RST at daytime with a tendency that both indices on S1 and S3 were higher than those on S2 and S4 (Figures 6a and 8b). In addition, road width could contribute to this SVF distribution. For example, Sejong-daero has a width of 100 m, with no high-rise buildings, so there is no way to block sky (Figure 2).
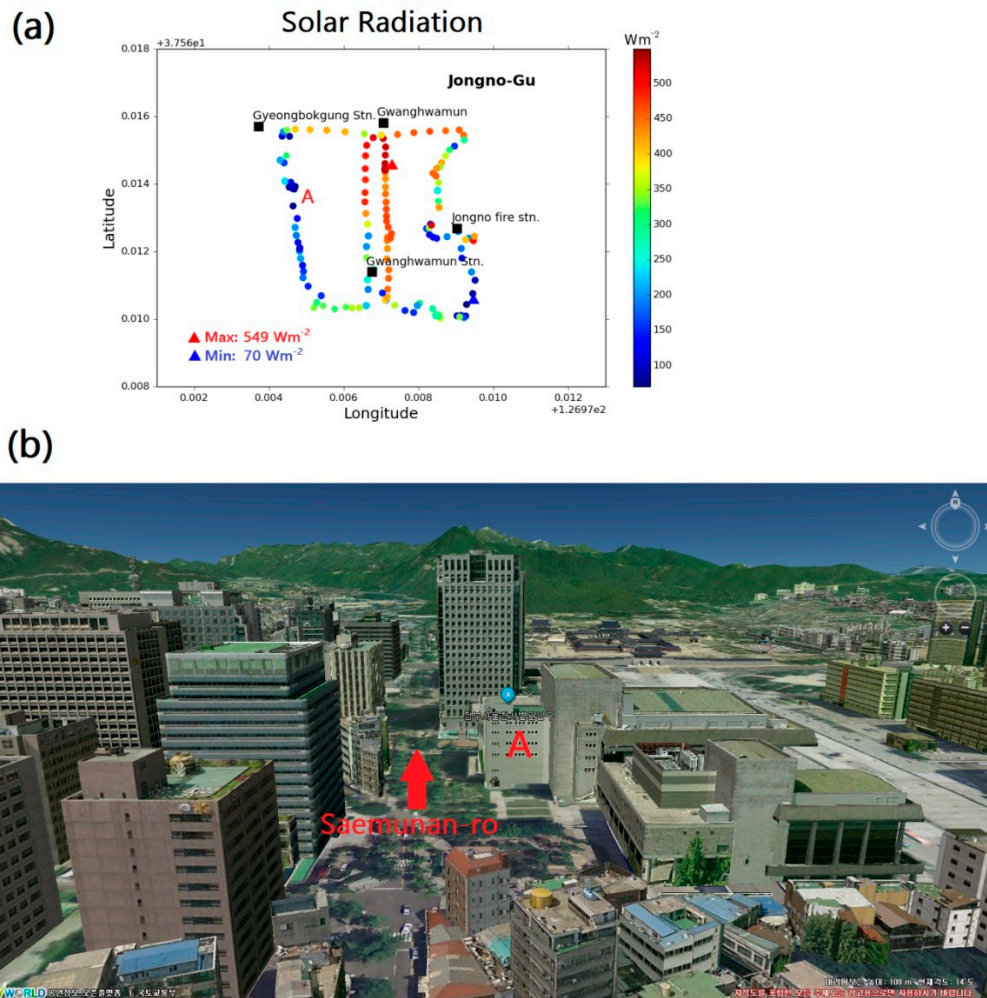

Figure 7. (**a**) Spatial distribution of solar radiation from MOVE observation during the daytime (1547–1602 LST) on 6 August, 2019, and (**b**) a 3D map view in the section of Saemunan-ro 5-gil from Vworld web service.

We further investigated the quantitative relationship between geometric properties, mainly SVF and RST, in four sections with different local features. Figure 9a shows averaged values of RST and SVF for four different sections with the error bars denoting the standard deviations. As a result, in all sections, the averaged SVF showed a similar tendency compared with that of RST: the higher the SVF, the higher the RST, and the lower the SVF, the lower the RST. As expected, the highest SVF (0.85) and RST (47.2 °C) were observed in S1, whereas the lowest SVF (0.47) and RST (39.2 °C) were observed in S2, with significant differences of 0.38 and 8 °C, respectively. Finally, it is worthwhile seeing the relationship between RST and SVF in Figure 9b. Overall, these data exhibit a positive correlation with a separately clustered pattern, such that roads in S1 have greater RST and SVF, whereas roads in S2 have less RST and SVF (the order of S1 > S3 > S4 > S2). In general, the greater SVFs are generally coincident with the greater RSTs, with a significant correlation ($R^2 = 0.91$), which indicates that RST seems to be

associated with SVF in terms of the averaging of each section. Statistical measures of the regression line for the scatter plot indicate a *p*-value of 0.044, which implies statistical significance at the 5% level. A notable attribute of this observational analysis is that urban street surfaces are increasingly heating as the SVF is increased. That is, we suggest that the SVF could influence the RST in hottest time of urban areas, whereas incoming solar radiation contributes indirectly to the magnitude of RST, since it is dependent on diurnal variations in solar altitude and azimuth angles.
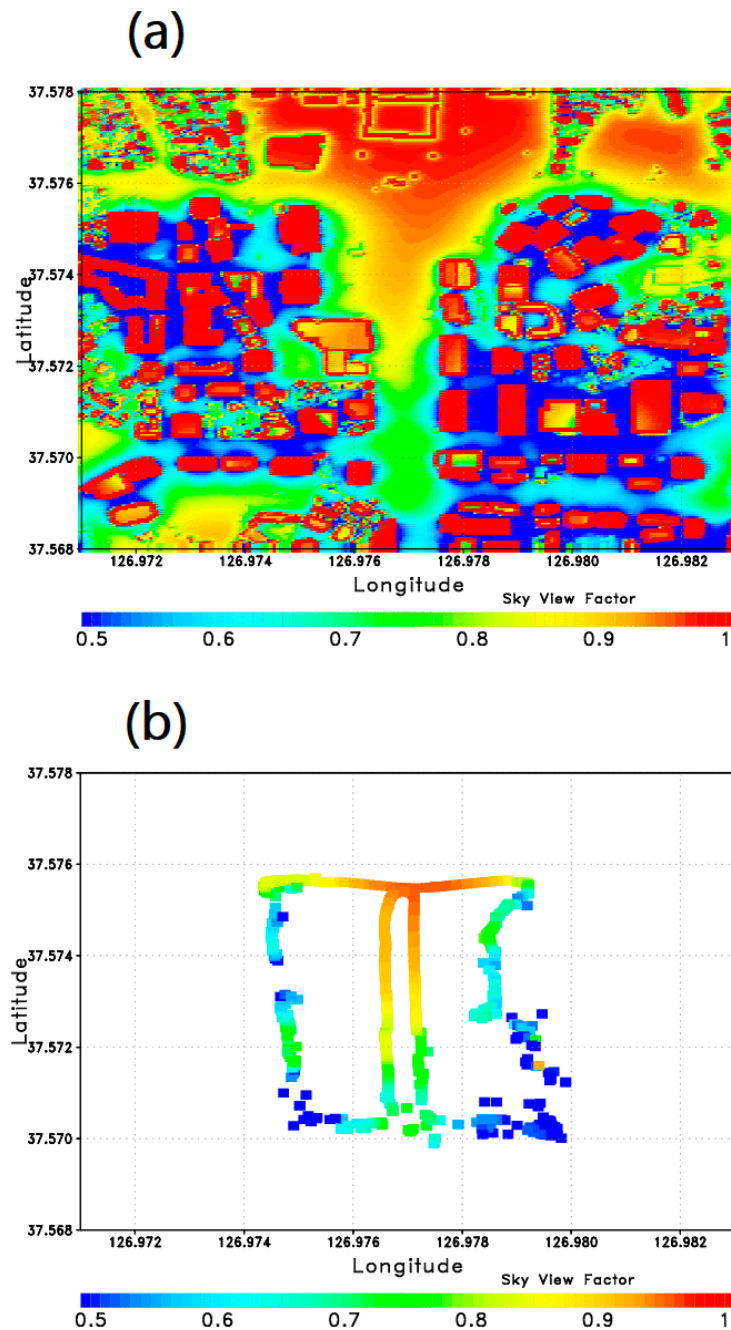
Figure 8. Sky view factor (SVF) distributions retrieved from digital surface model (DSM) (**a**) in the study area and (**b**) on the observation route of MOVE.
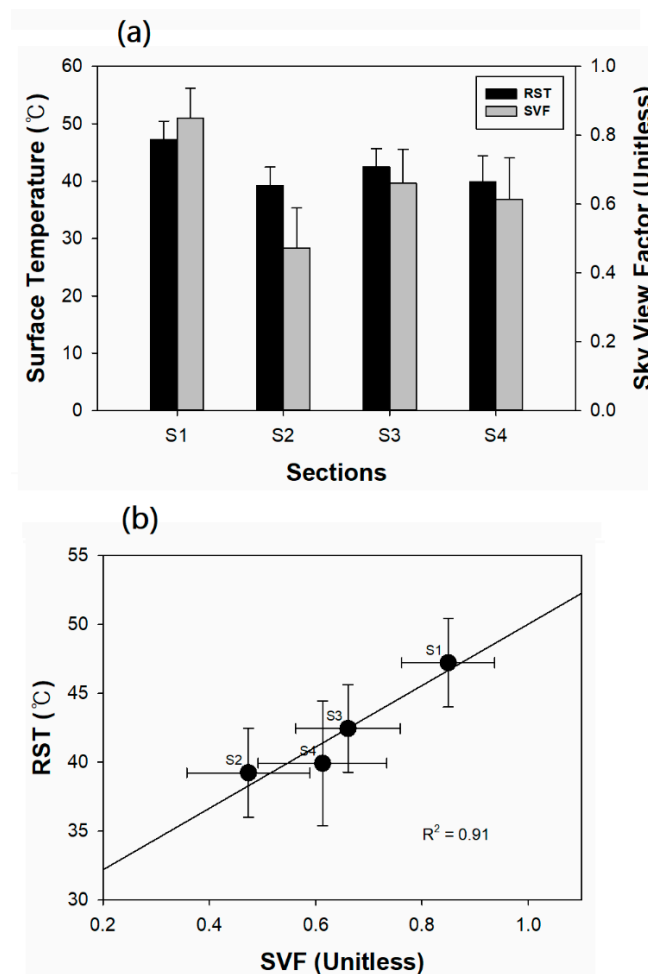
Figure 9. (**a**) The mean and standard deviations of road surface temperature (RST) and sky view factor (SVF) for the different sections, and (**b**) relationship of SVF to RST. The horizontal and vertical error bars denote standard deviations of RST and SVF, respectively.

4.4. Diurnal Variations

To further the current knowledge of RST, the current section proposes studying the diurnal variations of the air temperature and RST as well as diurnal temperature range (DTR) behavior on urban streets with different surrounding environments, distributed throughout Gwanghwamun. The main objective is to investigate local features of urban street and to draw diurnal trend plots, where markers have been traced with intervals of about 30 min, except for dawn time (from 2115 LST on 5 August to 0647 LST on 6 August). To achieve this, observed MOVE data with high temporal resolution during the BBMEX campaign were analyzed in different road sections. Figure 10a shows the diurnal variation of air temperature for the different road sections along with site R1 (Gwanghwamun Square). We calculated the mean and standard deviation values of air temperature at each section, and then presented them as time series, as shown in Figure 10a and Table 4. The time series show significant differences in the observed air temperature during the hottest hours (1547–1621 LST on 6 August) between S1 and the other sections with a maximum difference of 1.3 °C, despite both S1 and the other air temperatures reaching parity during the nocturnal hours. Compared to site R1, the air temperature in S1 well captures maximum (38.0 °C) and minimum (30.2 °C) temperatures with peak time as well as diurnal variation. That is, S1 means the hottest section as with reference site (R1) during the whole day. S1 and R1 temperatures only differ by 0.1–1.1 °C during the BBMEX campaign. However, the air temperature in S4 is relatively cooler than that of the other sections, which corresponds well with the presence of trees on both sides of the road, as shown in Figure 2. The four urban street

sections experience minimum air temperatures at least 29.4 °C (tropical night phenomenon) during the nighttime, which is commonly attributed to increased thermal storage, thereby amplifying the urban heat island (UHI) effect [46]. One thing to note is that the air temperatures have temperature differences within 0.5 °C and low variability, with a standard deviations of 0.08–0.34 °C, during the nighttime and early morning hours (Table 4).
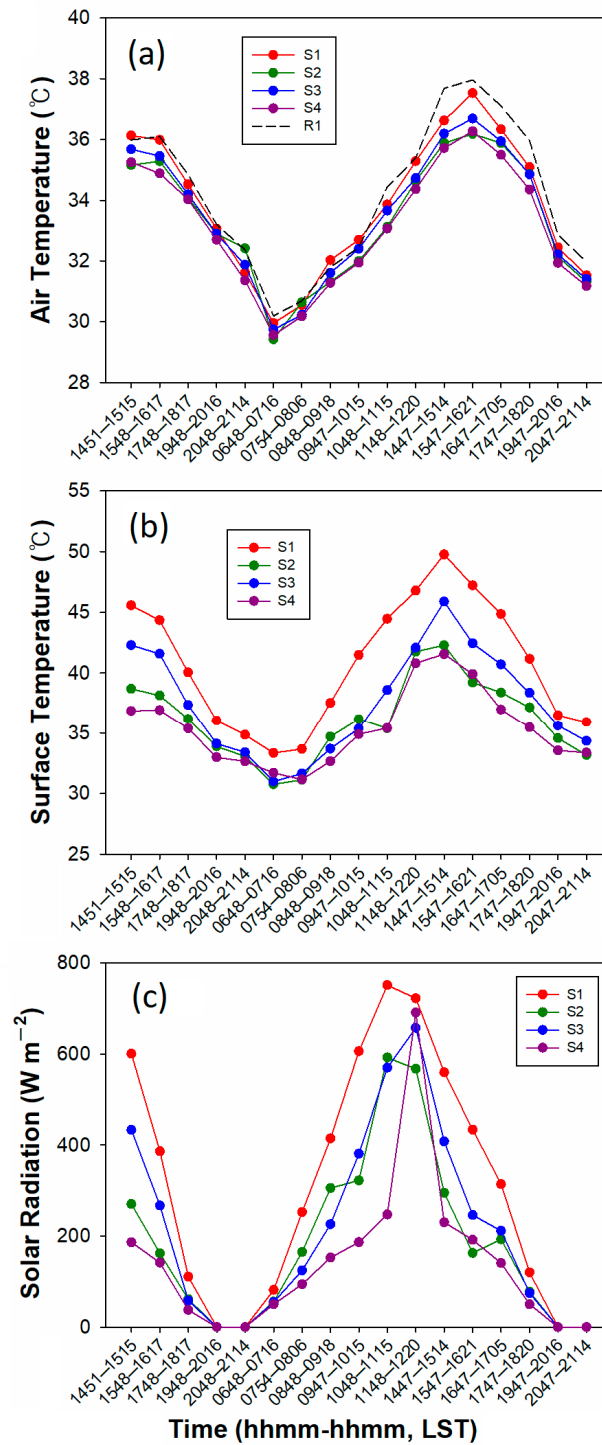
Figure 10. Diurnal variations of (**a**) air temperature, (**b**) road surface temperature (RST) and (**c**) solar radiation for the different sections. R1 with black dashed line in Figure 10a denotes air temperature of reference site.

Table 4. Statistics of air temperatures for each section during the BBMEX campaign.

Time (LST)	S1		S2		S3		S4		R1 *	
	Ave. **	Std. **	Ave.	Std.	Ave.	Std.	Ave.	Std.	Ave.	Std.
1451–1515	36.1	0.71	35.2	0.18	35.7	0.48	35.3	0.44	36.0	0.26
1548–1617	36.0	0.48	35.3	0.27	35.5	0.35	34.9	0.22	36.1	0.16
1748–1817	34.5	0.43	34.1	0.13	34.2	0.26	34.0	0.24	34.8	0.15
1948–2016	33.1	0.54	32.9	0.30	32.9	0.30	32.7	0.21	33.2	0.15
2048–2114	31.6	0.49	32.4	0.18	31.9	0.46	31.4	0.18	32.4	0.26
0648–0716	30.0	0.33	29.4	0.08	29.7	0.18	29.6	0.15	30.2	0.13
0754–0806	30.5	0.38	30.6	0.24	30.2	0.16	30.2	0.31	30.7	0.06
0848–0918	32.0	0.61	31.3	0.22	31.6	0.31	31.3	0.48	31.8	0.17
0947–1015	32.7	0.48	32.0	0.43	32.4	0.37	31.9	0.22	32.4	0.17
1048–1115	33.9	0.59	33.1	0.26	33.7	0.39	33.1	0.17	34.4	0.15
1148–1220	35.3	0.68	34.6	0.27	34.7	0.28	34.4	0.27	35.4	0.15
1447–1514	36.6	0.50	35.9	0.34	36.2	0.40	35.7	0.14	37.7	0.43
1547–1621	37.5	0.69	36.2	0.30	36.7	0.56	36.3	0.35	38.0	0.20
1647–1705	36.3	0.58	35.9	0.39	35.9	0.51	35.5	0.41	37.1	0.28
1747–1820	35.1	0.50	34.9	0.17	34.8	0.36	34.4	0.22	36.0	0.27
1947–2016	32.4	0.44	32.1	0.15	32.2	0.19	31.9	0.17	32.9	0.16
2047–2114	31.5	0.34	31.3	0.15	31.4	0.14	31.2	0.14	32.0	0.11

* R1 denotes reference site near Gwanghwamun Square. ** Units are °C.

The increase in RST is mainly due to the replacement of natural land cover with built materials like concrete and asphalt that lack moisture retention capacity but have high thermal storage capacity [47]. The materials overwhelmingly redistribute the incoming solar energy into sensible heat, thereby disproportionately increasing urban RST [48]. The majority of the road material in the study area (Gwanghwamun) is covered by asphalt: nearly 97%, except for some Sejong-daero section with concrete blocks (3%). Therefore, we did not consider different urban street materials to have distinctly different RST. These differences are assumed to be determined only by different thermal environments around each urban street. Figure 10b shows the diurnal cycle of RST during the BBMEX campaign. As expected, the RST in S1 is higher than that of the other sections with mean differences of ranging from 3.2 °C to 5.4 °C (Table 5), which is most dependent on the degree of sky openness. The comparison shows that the RSTs in S2 and S4 were around 4.6 °C and 5.4 °C cooler than that of S1 in the daily average perspective; the densities of high-rise buildings and street trees are primarily responsible for this magnification. In this regard, the amount of solar radiation that a street receives largely depends on urban geometry such as trees and buildings. Therefore, we also analyzed the diurnal variations of solar radiation as shown in Figure 10c. The solar radiation is mostly correlated with RST, while sunshine depends on the four different sections. These results suggest that the diurnal cycle of RST is driven by surface solar radiation. Because urban geometry can greatly modulate the solar radiation reaching the surface, it has the greatest influence on RST. Compared to the air temperature trend, the diurnal variation of RST seemed to be similar despite the large standard deviations (up to 4.8 °C during the daytime). However, the peak time of maximum for both temperatures was somewhat different. It is interesting to note that the time lag between the observed maximum air temperature and RST was about one hour, which may be attributable to an increase in air temperature induced by an increase in RST. That is, impervious road materials such as asphalt and concrete absorb and store large amounts of heat, thereby increasing the RSTs, which increase air temperature above artificial pavement through heat convection with some latency [49]. On the other hand, the signature of the difference field between air temperature and RST exhibits a result similar to that of the diurnal variation of RST. This phenomenon can be interpreted as a result of large fluctuations in RST, while diurnal variation of air temperature has low variability.

Table 5. The same as in Table 4 except for road surface temperatures (RSTs).

Time (LST)	S1		S2		S3		S4	
	Ave.	Std.	Ave.	Std.	Ave.	Std.	Ave.	Std.
1451–1515	45.6	3.35	38.7	3.29	42.3	3.35	36.9	2.92
1548–1617	44.4	3.04	38.1	2.64	41.6	2.62	36.9	2.17
1748–1817	40.1	2.02	36.2	1.73	37.4	1.46	35.4	1.79
1948–2016	36.1	1.02	33.9	1.08	34.1	0.83	33.0	1.34
2048–2114	34.9	0.92	33.1	1.04	33.4	0.76	32.6	0.78
0648–0716	33.3	0.93	30.8	1.27	31.0	1.33	31.7	0.63
0754–0806	33.7	1.37	31.1	1.09	31.6	1.00	31.2	0.63
0848–0918	37.5	2.68	34.7	2.32	33.7	1.70	32.6	1.63
0947–1015	41.5	3.54	36.2	3.60	35.4	3.91	34.9	3.74
1048–1115	44.5	3.41	35.4	4.07	38.6	4.74	35.4	4.41
1148–1220	46.8	2.01	41.8	2.80	42.1	4.20	40.8	3.43
1447–1514	49.8	3.59	42.3	4.19	45.9	3.48	41.6	4.84
1547–1621	47.2	3.21	39.2	3.23	42.5	3.18	39.9	4.52
1647–1705	44.9	1.86	38.4	2.80	40.7	2.43	37.0	3.02
1747–1820	41.2	1.97	37.2	1.76	38.4	1.38	35.5	1.34
1947–2016	36.5	1.34	34.6	1.19	35.6	1.07	33.5	0.88
2047–2114	35.9	1.02	33.2	0.92	34.3	0.91	33.4	0.68

DTR is a fundamental component of the climate system, and changes in its pattern can affect human health, ecosystems, plants and renewable energy systems, etc. [50]. Therefore, research into DTR variability on regional and local urban scales is vital. This study highlights the differences according to RST, air temperature and temperature difference from the point of view of DTR at each road section. Figure 11 shows DTRs of RST, air temperature and temperature difference for different sections. First, there were significant differences in DTR of RST between all of the sections. The DTRs of RST in S2 and S4 were relatively smaller than that of S1 and S3, with differences of ranging from 2.9 °C to 4.5 °C. It can be seen that the much higher urban canopy with high-rise buildings in S2 and S4 effect the maximum RST compared with S1 and S3. Especially in S4, this magnitude of DTR in RST was the smallest (10.4 °C). This is to be expected, because S4 not only has a larger building density in general, and thus reflects more sunlight and reduces the maximum RST more efficiently than S1 or S3, but it also has a higher urban tree canopy, such that it has the potential to dampen the DTR and decrease RST through direct shading and evaporative cooling [51]. On the other hand, the magnitude of DTR in air temperature generally follows the order of S1 (7.6 °C) > S3 (7.0 °C) > S2 (6.8 °C) > S4 (6.7 °C), like the RST, although the DTR of S4 is slightly lower than that in the other sections, a difference of within 0.9 °C (Figure 11). The characteristics of DTRs in RST and air temperature are consistent with correlative relationships discussed above (cf. Figure 10). The DTR in temperature difference also correlates with that of RST, because of its dependence on the change rate of DTR. Based on our investigation, the decreased RST decreases the maximums in RST and air temperature during the daytime, resulting in a relatively large DTR reduction compared with the increased RST. In summary, the above comparative results suggest that the diurnal variation and DTR in RST and air temperature are driven by the thermal environmental characteristics of urban streets.

In S4, the lowest RST and air temperature are observed on the diurnal variation, which is shown in Figure 10 (also Tables 4 and 5). To identify the relationships between those temperatures and specific humidity on diurnal variations, we used the further dataset of air pressure and relative humidity observed from MOVE. As mentioned previously, specific humidity can be calculated using the above variables, which is a useful indicator, because the rate of evapotranspiration of water from any surface is directly proportional to their difference between the surface and the adjoining air. Figure 12 shows the diurnal variation of averaged specific humidity calculated at each section. As a result, specific humidity remained high (greater than 16 g kg^{-1}) in the early period, and starting from 0754–0806 LST on 6 August, it rapidly decreased until 1447–1514 LST (less than 13 g kg^{-1}) and then gradually restored

again to 15 g kg^{-1}. These patterns are correlated with the diurnal variation of RST with a tendency to be out of phase. When the RST is the highest (1447–1514 LST), it can be seen that the specific humidity decreases rapidly down to 12.6 g kg^{-1}, whereby it is likely that the increasing RST may have contributed to the humidity changes, especially on the urban streets mostly covered by asphalt (97%). Additionally, low humidity is not good at absorbing in the near-infrared part of solar radiation, which increases the amount of daytime energy reaching the surface with negative feedback. However, there were no significant differences in specific humidity between S4 and the other sections (Figure 12). It should be pointed out that the tree shading effect in S4 should depend more on the changes of RST and air temperature than the evaporative cooling effect, because the above specific humidity is not a dominant factor in S4, probably due to the fact that insufficient street trees and dryness of soil moisture may have weakened lowering RST and ambient air temperature through evapotranspiration.
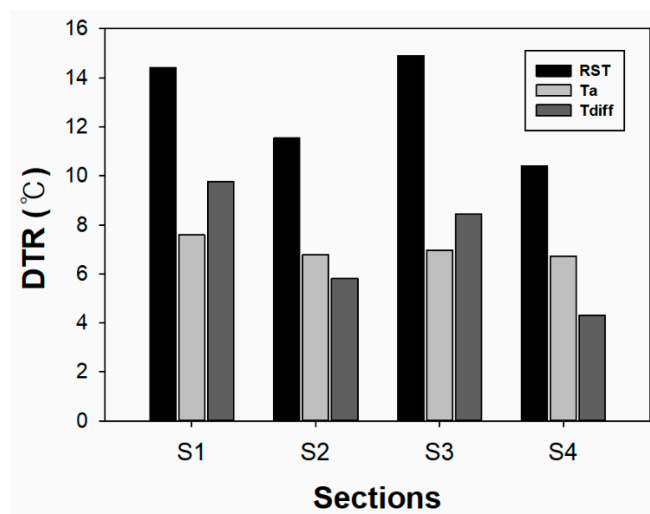

Figure 11. Diurnal temperature ranges (DTRs) of road-surface temperature (RST), air temperature (Ta) and temperature difference (Tdiff) for different sections.
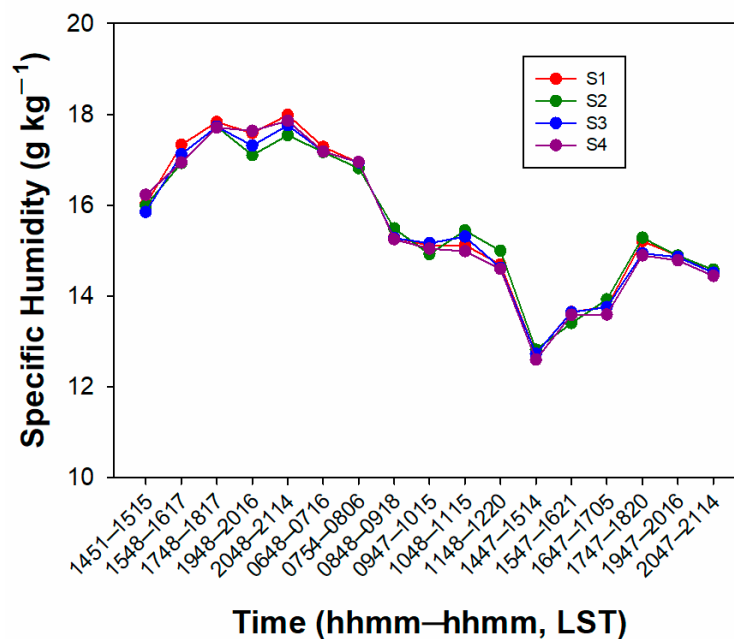

Figure 12. The same as in Figure 10, except for specific humidity.

5. Discussion

In this study, we investigated the characteristics of thermal environments and diurnal variations of road surface temperature (RST) and air temperature, particularly at the urban street level, during the 2019 Building Block 3-dimensional urban Meteorological Experiment (BBMEX) campaign in Seoul. An intensive observation dataset of mobile observation vehicle (MOVE), with high spatial and temporal resolutions, for the heat wave episode that occurred on 5–6 August 2019 were used to analyze the relationship between RST and sky view factor (SVF), and other relevant factors in terms of field observational analysis. For the purpose of comparing characteristics of RST and air temperature with different surrounding thermal environments, we divided the study area into four road sections as follows: S1: Open Section, S2: High-Rise Buildings, S3: Low-Rise Buildings, and S4: Street Trees.

The results showed that the greater SVFs were generally coincident with the greater RSTs, with a significant correlation ($R^2 = 0.91$), which indicates that RST seems to be associated with SVF in terms of the averaging of each section. Statistical measures of the regression line for scatter plot indicate a *p*-value of 0.044, which implies statistical significance at the 5% level. It is interesting to note that the time lag between observed maximum air temperature and RST was about one hour, which may be attributable to an increase in air temperature induced by an increase in RST. The DTRs of RST in S2 and S4 were relatively smaller than that of S1 and S3, with differences ranging from 2.9 °C to 4.5 °C. Especially in S4, this magnitude of DTR in RST was the smallest (10.4 °C), which is expected because S4 not only has greater building density, but also has a higher urban tree canopy, thereby having the potential to dampen the DTR. However, there were no significant differences in specific humidity between S4 and the other sections.

Despite these findings, this research has limitations insofar as it only focused on one heat wave episode, which prohibits generalization to temperature changes on urban streets mostly covered by same surface material (asphalt) at different locations. A comparative case study with four different urban streets is investigated in the current research. Since limited urban street elements affecting urban thermal environments and diurnal variations were found in the study area herein, expanding this study to elsewhere to obtain more reliable information about the effects of certain urban elements is required. In addition, it is necessary to consider the effects of various environmental indices or radiation/meteorological factors on diurnal variations of urban street elements, such as floor area ratio, Bowen ratio, traffic volume, surface emissivity, clouds, winds, etc. [52–54]. The RST and air temperature vary in complex environments, like urban areas. Thus, the integration of numerical prediction models, road weather information systems (RWISs), and MOVE observations is required to provide better thermal mapping information on urban streets [9].

6. Conclusions

This study emphasizes the characteristics of diurnal variations in actual RST and air temperature observed from the MOVE platform in urban areas on heat wave days. Moreover, the results of our study were robust, with advanced observation techniques and a sufficient number of samples, while capturing the effects of spatial correlation. Our findings indicate that the characteristics of different thermal environmental indices and diurnal variations should be considered to reduce the RST and mitigate the urban heat island and heat wave effects. More specifically, based on the findings of this study, in order to create better thermal environments of urban streets for drivers, road surface materials with high albedo values and cool pavements [8,55–57] should be used, and shading effects from street trees and water-sprinkling effects should be optimized. These strategies should be considered primarily in urban areas where drivers are exposed to extreme heat stress [15]. Although this approach has a couple of limitations, the current results could be used in the preliminary stages of further studies, and will assist planners and decision makers in determining policy priorities (e.g., planting urban trees and water-sprinkling) for improving urban thermal environments with regard to urban street design and planning. In the future, we plan to utilize a spherical camera with 360° field of view (like Google

Street View) installed on a MOVE platform in order to provide better SVF mapping information, as addressed by Honjo et al. (2019) [58].

References

1. Barnett, A.G. Temperature and cardiovascular deaths in the US elderly: Changes over time. *Epidemiology* **2007**, *18*, 369–372. [CrossRef] [PubMed]
2. Schubert, S.D.; Wang, H.; Koster, R.D.; Suarez, M.J. Northern Eurasian heat waves and droughts. *J. Clim.* **2014**, *27*, 3169–3207. [CrossRef]
3. Kim, D.-W.; Deo, R.C.; Lee, J.-S.; Yeom, J.-M. Mapping heatwave vulnerability in Korea. *Nat. Hazards* **2017**, *89*, 35–55. [CrossRef]
4. McCarthy, M.P.; Best, M.J.; Betts, R.A. Climate change in cities due to global warming and urban effects. *Geophys. Res. Lett.* **2010**, *37*, L09705. [CrossRef]
5. Papanastasiou, D.K.; Melas, D.; Bartzanas, T.; Kittas, C. Temperature, comfort and pollution levels during heat waves and the role of sea breeze. *Int. J. Biometeorol.* **2010**, *54*, 307–317. [CrossRef] [PubMed]
6. Ha, K.J.; Yun, K.S. Climate change effects on tropical night days in Seoul, Korea. *Theor. Appl. Climatol.* **2012**, *109*, 191–203. [CrossRef]
7. Campbell, F.C. *Elements of Metallurgy and Engineering Alloys*; OCLC 608624525; ASM International: Materials Park, OH, USA, 2008; ISBN 9780871708670.
8. Synnefa, A.; Karlessi, T.; Gaitani, N. Experimental testing of cool colored thin layer asphalt and estimation of its potential to improve the urban microclimate. *Build. Environ.* **2010**, *46*, 38–44. [CrossRef]
9. Kim, Y.-J.; Kim, B.-J.; Shin, Y.-S.; Kim, H.-W.; Kim, G.-T.; Kim, S.-J. A case study of environmental characteristics on urban road-surface and air temperatures during heat-wave days in Seoul. *Atmos. Ocean. Sci. Lett.* **2019**, *12*, 261–269. [CrossRef]
10. Bae, W.K.; Yoon, K.H. A design guideline of the apartment house complex for mitigation of heat island effect–For the planning agenda constructed and elected in 2005–2010. *J. Archit. Inst. Korean Plan.* **2012**, *13*, 47–60.
11. Chung, M.H.; Park, J.C. Development of PCM cool roof system to control urban heat island considering temperate climatic conditions. *Energy Build.* **2016**, *116*, 248–341. [CrossRef]
12. Jeong, J.; Chung, M.H. The planning of micro-climate control by complex types. *Int. J. Korea Inst. Ecol. Archit. Environ.* **2017**, *17*, 49–54. [CrossRef]
13. Yamazaki, F.; Murakoshi, A.; Sekiya, N. Observation of urban heat island using airborne thermal sensors. In Proceedings of the 2009 Joint Urban Remote Sensing Event, Shanghai, China, 20–22 May 2009.
14. Yoon, J. Field measurement recorded in the urban thermal environment of a medium-size city in autumn and winter. *J. Archit. Inst. Korea Plan.* **2009**, *25*, 453–460.
15. Lee, S.; Moon, H.; Choi, Y.; Yoon, D.K. Analyzing thermal characteristics of urban streets using a thermal imaging camera: A case study on commercial streets in Seoul, Korea. *Sustainability* **2018**, *10*, 519. [CrossRef]
16. Ibrahim, F. Urban land use land cover changes and their effect on land surface temperature: Case study using Dohuk City in the Kurdistan Region of Iraq. *Climate* **2017**, *5*, 13. [CrossRef]
17. Zhang, X.; Estoque, R.C.; Murayama, Y. An urban heat island study in Nanchang City, China based on land surface temperature and social-ecological variables. *Sustain. Cities Soc.* **2017**, *32*, 557–568. [CrossRef]

18. Zhao, Z.-Q.; He, B.-J.; Li, L.-G.; Wang, H.-B.; Darko, A. Profile and concentric zonal analysis of relationships between land use/land cover and land surface temperature: Case study of Shenyang, China. *Energy Build.* **2017**, *155*, 282–295. [CrossRef]

19. Yang, K.; Yu, Z.; Luo, Y.; Yang, Y.; Zhao, L.; Zhou, X. Spatial and temporal variations in the relationship between lake water surface temperatures and water quality–A case study of Dianchi Lake. *Sci. Total Environ.* **2018**, *624*, 859–871. [CrossRef]

20. He, B.-J.; Zhao, Z.-Q.; Shen, L.-D.; Wang, H.-B.; Li, L.-G. An approach to examining performances of cool/hot sources in mitigating/enhancing land surface temperature under different temperature backgrounds based on landsat 8 image. *Sustain. Cities Soc.* **2019**, *44*, 416–427. [CrossRef]

21. Shao, J.; Swanson, J.C.; Patterson, R.; Lister, P.J.; McDonald, A.N. Variation of winter road surface temperature due to topography and application of thermal mapping. *Meteorol. Appl.* **1997**, *4*, 131–137. [CrossRef]

22. Bogren, J.; Gustavsson, T.; Karlsson, M.; Postgård, U. The impact of screening on road surface temperature. *Meteorol. Appl.* **2000**, *7*, 97–104. [CrossRef]

23. Postgård, U.; Lindqvist, S. Air and road surface temperature variations during weather change. *Meteorol. Appl.* **2001**, *8*, 71–84. [CrossRef]

24. Chao, J.; Zhang, J. Prediction model for asphalt pavement temperature in high-temperature season in Beijing. *Adv. Civ. Eng.* **2018**, 1–11. [CrossRef]

25. Dai, A.; Kevin, E.T.; Thomas, R.K. Effects of clouds, soil moisture, precipitation, and water vapor on diurnal temperature range. *J. Clim.* **1999**, *12*, 2451–2473. [CrossRef]

26. Liu, W.; Feddema, J.; Hu, L.; Zung, A.; Brunsell, N. Seasonal and diurnal characteristics of land surface temperature and major explanatory factors in Harris Country, Texas. *Sustainability* **2017**, *9*, 2324. [CrossRef]

27. Bilbao, J.; Román, R.; Miguel, A.D. Temporal and spatial variability in surface air temperature and diurnal temperature range in Spain over the period 1950–2011. *Climate* **2019**, *7*, 16. [CrossRef]

28. Grimmond, S. Urbanization and global environmental change: Local effects of urban warming. *Geogr. J.* **2007**, *173*, 83–88. [CrossRef]

29. Unger, J. Connection between urban heat island and sky view factor approximated by a software tool on a 3D urban database. *Int. J. Environ. Pollut.* **2008**, *36*, 59–80. [CrossRef]

30. Ha, J.; Lee, S.; Park, C. Temporal effects of environmental characteristics on urban air temperature: The influence of the sky view factor. *Sustainability* **2016**, *8*, 895. [CrossRef]

31. Solaimanian, M.; Kennedy, T.W. Predicting maximum pavement surface temperature using maximum air temperature and hourly solar radiation. *Transp. Res. Rec.* **1993**, *1417*, 1–11.

32. Offerle, B.; Eliasson, I.; Grimmond, C.S.B. Surface heating in relation to air temperature, wind and turbulence in an urban street canyon. *Bound. Layer Meteorol.* **2007**, *122*, 273–292. [CrossRef]

33. Park, M.-S.; Park, S.-H.; Chae, J.-H.; Choi, M.-H.; Song, Y.; Kang, M.; Roh, J.-W. High-resolution urban observation network for user-specific meteorological information service in the Seoul Metropolitan Area, South Korea. *Atmos. Meas. Tech.* **2017**, *10*, 1575–1594. [CrossRef]

34. World Meteorological Organization. *Guide to Meteorological Instruments and Methods of Observation*; WMO: Geneva, Switzerland, 1996; Available online: http://hdl.handle.net/11329/83 (accessed on 29 November 2019).

35. Kim, Y.-J.; Kim, S.-J.; Kim, G.-T.; Choi, B.-C.; Shim, J.-K.; Kim, B.-G. Retrieval and validation of precipitable water vapor using GPS datasets of mobile observation vehicle on the eastern coast of Korea. *Korean J. Remote Sens.* **2016**, *4*, 365–382. [CrossRef]

36. Chun, B.S.; Guldmann, J.M. Spatial statistical analysis and simulation of the urban heat island in high-density central cities. *Landsc. Urban Plan.* **2014**, *125*, 76–88. [CrossRef]

37. Bernard, J.; Bocher, E.; Petit, G.; Palominos, S. Sky view factor calculation in urban context: Computational performance and accuracy analysis of two open and free GIS tools. *Climate* **2018**, *6*, 60. [CrossRef]

38. Jee, J.-B.; Zo, I.-S.; Kim, B.-Y.; Lee, K.-T. An analysis of observational environments for solar radiation stations of Korea meteorological administration using the digital elevation model and solar radiation model. *J. Korean Earth Sci. Soc.* **2019**, *40*, 119–134, (In Korean with English abstract). [CrossRef]

39. Bolton, D. The computation of equivalent potential temperature. *Mon. Weather Rev.* **1980**, *108*, 1046–1053. [CrossRef]

40. He, B.-J.; Ding, L.; Prasad, D. Enhancing urban ventilation performance through the development of precinct ventilation zones: A case study based on the Greater Sydney, Australia. *Sustain. Cities Soc.* **2019**, *47*, 101472. [CrossRef]

41. Lindberg, F.; Holmer, B.; Thorsson, S. SOLWEIG 1.0—Modeling spatial variations of 3D radiant fluxes and mean radiant temperature in complex urban settings. *Int. J. Biometeorol.* **2008**, *52*, 697–713. [CrossRef]

42. Gál, T.; Lindberg, F.; Unger, J. Computing continuous sky view factors using 3D urban raster and vector databases: Comparison and application to urban climate. *Theor. Appl. Climatol.* **2009**, *95*, 111–123. [CrossRef]

43. Kastendeuch, P.P. A method to estimate sky view factors from digital elevation models. *Int. J. Climatol.* **2013**, *33*, 1574–1578. [CrossRef]

44. Hämmerle, M.; Gál, T.; Unger, J.; Matzarakis, A. Comparison of models calculating the sky view factor used for urban climate investigations. *Theor. Appl. Climatol.* **2011**, *105*, 521–527. [CrossRef]

45. Jee, J.-B.; Yang, H.-J.; Lee, C.-Y.; Min, J.-S.; Kang, M.-S. Comparison of surface characteristics information retrievals and simulation of detailed temperature and wind field distributions using digital DSM and 3D camera image. In Proceedings of the Autumn Meeting of KMS 2019, Seoul, South Korea, 25–27 October 2019.

46. Ramamurthy, P.; Jorge, G.; Luis, O.; Mark, A.; Fred, M. Impact of heatwave on a megacity: An observational analysis of New York City during July 2016. *Environ. Res. Lett.* **2017**, *12*, 054011. [CrossRef]

47. Ramamurthy, P.; Bou-Zeid, E.; Wang, Z.; Smith, J.; Baek, M.; Welty, C.; Hom, J.; Saliendra, N. Influence of sub-facet heterogeneity and matrial properties on the urban surface energy budget. *J. Appl. Meteorol. Climatol.* **2014**, *53*, 2114–2129. [CrossRef]

48. Li, D.; Bou-Zeid, E. Synergistic interactions between urban heat island and heat waves: The impact in cities is larger than the sum of its parts. *Environ. Res. Lett.* **2013**, *52*, 2051–2064. [CrossRef]

49. Doulos, L.; Santamouris, M.; Livada, I. Passive cooling of outdoor urban spaces. The role of materials. *Sol. Energy* **2004**, *77*, 231–249. [CrossRef]

50. McMichael, A.J.; Campbell-Lendrum, D.H.; Corvalán, C.F.; Ebi, K.L.; Githeko, A.K.; Scheraga, J.D.; Woodward, A. *Climate Change and Human Health: Risks and Responses*; World Health Organization: Geneva, Switzerland, 2003; ISBN 92-4-1-56248-X.

51. Loughner, C.P.; Allen, D.J.; Zhang, D.-L.; Pickering, K.E.; Dickerson, R.R.; Landry, L. Roles of urban tree canopy and buildings in urban heat island effects: Parameterization and preliminary results. *J. Appl. Meteorol. Clim.* **2012**, *51*, 1775–1793. [CrossRef]

52. Kwak, K.-H.; Lee, S.-H.; Seo, J.M.; Park, S.-B.; Baik, J.-J. Relationship between rooftop and on-road concentrations of traffic-related pollutants in a busy street canyon: Ambient wind effects. *Environ. Pollut.* **2016**, *208*, 185–197. [CrossRef]

53. Kwak, K.-H.; Woo, S.H.; Kim, K.H.; Lee, S.-B.; Bae, G.-N.; Ma, Y.I.; Sunwoo, Y.; Baik, J.-J. On-road air quality associated with traffic composition and street-canyon ventilation: Mobile monitoring and CFD modeling. *Atmosphere* **2018**, *9*, 92. [CrossRef]

54. Luo, Y.; Li, Q.; Yang, K.; Xie, W.; Zhou, X.; Shang, C.; Xu, Y.; Zhang, Y.; Zhang, C. Thermodynamic analysis of air-ground and water-ground energy exchange process in urban space at micro scale. *Sci. Total Environ.* **2019**, *694*, 133612. [CrossRef]

55. Sailor, D.J. Simulated urban climate response to modifications in surface albedo and vegetative cover. *J. Appl. Meteorol.* **1995**, *34*, 1694–1704. [CrossRef]

56. Pomerantz, M.; Pon, B.; Akbari, H.; Chang, S.C. *The Effect of Pavements' Temperatures on Air Temperatures in Large Cities*; LBNL-43442; Lawrence Berkeley National Laboratory: Berkeley, CA, USA, 2000.

57. Guan, K.K. Surface and ambient air temperatures associated with different ground materials: A case study at the university of California, Berkeley. *Environ. Sci.* **2011**, *196*, 1–14.

58. Honjo, T.; Lin, T.-P.; Seo, Y. Skyview factor measurement by using a spherical camera. *J. Agric. Meteorol.* **2019**, *75*, 59–66. [CrossRef]